PHYSICAL REVIEW B **80**, 104102 (2009)

Nanoscale abnormal grain growth in (001) epitaxial ceria

Vyacheslav F. Solovyov*
Condensed Matter Physics and Materials Science Department, Brookhaven National Laboratory, Upton, New York 11973, USA

Katherine Develos-Bagarinao
National Institute of Advanced Industrial Science and Technology (AIST), Tsukuba Central 2, 1-1-1 Umezono Tsukuba, Ibaraki 305-8568, Japan

Dmytro Nykypanchuk
Center for Functional Nanomaterials, Brookhaven National Laboratory, Upton, New York 11973, USA

(Received 2 April 2009; published 4 September 2009)

X-ray reciprocal-space mapping and atomic force microscopy (AFM) are used to study kinetics and mechanisms of lateral grain growth in epitaxial (001) ceria (CeO_2) deposited by pulsed laser deposition on (001) yttria-stabilized zirconia (YSZ) and $(1\underline{2}10)$ (r-cut) sapphire. Rate and character of the grain growth during postannealing at 1050 °C are found to be strongly dependent on the type of the epitaxial substrate. Films deposited on YSZ exhibit signatures of normal grain growth, which stagnated after the lateral grain size reaches 40 nm, consistent with the grain-boundary pinning by the thermal grooving. In contrast, when r-cut sapphire substrate was used, abnormal (secondary) grain growth is observed. A small population of grains grow to well over 100 nm consuming smaller, <10 nm, grains, thus forming well-defined >100 nm large (001) terminations and rendering the sample single-crystalline quality. The grain growth is accompanied by reduction in lateral rms strain, resulting in a universal grain size—rms strain dependence. Analysis of the AFM and x-ray diffraction data leads to the conclusion that bimodal initial grain population consisting of grains with very different sizes is responsible for initiation of the abnormal growth in (001) CeO_2 films on r-cut sapphire. Due to different surface chemistry, when a YSZ substrate is used, the initial grain distribution is monomodal, therefore only normal growth is active. We demonstrate that a 2.2° miscut of the sapphire substrate eliminates the large-grain population, thus suppressing abnormal grain growth. It is concluded that utilization of abnormal grain growth is a promising way for synthesis of large (001) ceria terminations.

DOI: 10.1103/PhysRevB.80.104102 PACS number(s): 61.72.Dd, 61.72.Cc, 61.72.Mm, 68.37.Ps

I. INTRODUCTION

Cerium oxide films find various applications as a catalyst,[1–3] a template layer for epitaxial growth of complex oxides, and a diffusion barrier. In many applications, CeO_2 is deposited as a thin (<0.1 μm) epitaxial layer on an appropriate substrate. If a (001) film is used as an epitaxial template, it is desirable to have a film with well-defined (001) surface termination. For example, (001)-oriented ceria layer is now widely used as a template for growth of a thick oriented layer of high-temperature superconductor, $YBa_2Cu_3O_7$, which is a critical component of the so-called second-generation superconducting wires. A template with low density or small (001) terminations would provide a low density of nucleation sites for the $YBa_2Cu_3O_7$ phase. As a consequence, other undesirable phases would be allowed to nucleate, reducing the structural quality of the film.[4]

The atomic arrangement on (001) face of ceria is such that the surface energy is approximately two times higher than the other low-index faces: (111) and (110). The high energy of the (001) face has been theoretically explained by weak bonding of the O^{2-} ion to (100) surface,[5,6] which has been confirmed experimentally.[7] Given the difference in surface energies of low-index faces, a Wulff construction[8,9] predicts that at equilibrium a ceria crystal would take the shape of a truncated octahedron with (111) planes being the primary terminations and (001) planes truncating the octahedron vertices.[10] A Wulff construction becomes inaccurate on the nanoscale level because the atomistic nature of crystal faces starts to play a significant role in the energy balance and packing corrections have to be introduced. Corrected Wulff plots for 10^4–10^9 atom clusters of a model cubic material were calculated by Marks;[11] it was shown that the surface fraction of (001) terminations gradually disappears as the cluster became smaller than 10^6 atoms. Indeed, it was observed that unsupported ceria particles less than 10 nm in diameter were (111) terminated octahedra with no (001) truncations.[12] The tendency for (111) termination of small ceria grain was also recognized in epitaxial (001) films: in films with small lateral grain size the surface was comprised of pyramidlike (111) facets.[13,14] Contrast between (100) and (111) ceria orientations has been emphasized by Wu *et al.*,[14] who compared CeO_2 epitaxy on (001) and (111) faces of yttria-stabilized zirconia (YSZ) single crystals. Films deposited on (111) YSZ face exhibited excellent flatness and crystallinity, while (001)-oriented films deposited under the same conditions on (001) YSZ face were invariably small grained and rough.

The termination problem in thin films can be traced to a small lateral grain size of ceria, which is explained by the very low free energy (−880 kJ/mol) of CeO_2 formation and, consequently, a high nucleation rate under typical physical vapor deposition conditions. Due to the very high melting temperature T_m of ceria (2600 °C), a practical deposition will be possible at a temperature well below $0.5T_m$. According to Thornton,[15] this is the so-called "zone T" deposition

 ©2009 The American Physical Society

regime, which produces films with small faceted grains. An as-deposited film can be postannealed to increase the grain size, improve the structural quality, and produce desired (001) terminations. Jacobsen *et al.*[13] have shown that the annealing step is capable of transforming at least some grains with (111) terminations into ones with (001) terminations. It was observed by Zaitsev *et al.*[16] and Develos-Bagarinao *et al.*[17] that CeO_2 on *r*-cut sapphire had much better out-of-plane alignment than CeO_2 films deposited under similar conditions on better-matched substrates such as YSZ,[14] $SrTiO_3$,[18] Ge,[19] or MgO,[20] suggesting that the sapphire substrate promoted lateral grain growth. It was also demonstrated that even initially small-grained CeO_2 film deposited on *r*-cut sapphire can be annealed into single-crystalline-like quality. This is especially surprising considering that *r*-cut sapphire surface has a large lattice mismatch with CeO_2: 3.7% and 12.1% along $[\underline{1}101]$ and $[11\underline{2}0]$ directions, respectively, at room temperature and 4.1% and 12.4% at 1000 °C. However, Chromik *et al.*[21] observed that the effect can vary significantly from one batch of sapphire substrates to another, implying that the substrate surface is responsible for the anomalous structure improvement.

In this work we use x-ray reciprocal-space mapping to explore the dynamics of lateral grain growth in CeO_2 films deposited on *r*-cut sapphire and (001) YSZ. Mapping of (*hkl*) reflections allows us to acquire reliable averaged information about grain structure and strain magnitude and arrive at a consistent quantitative description of the lateral structure. The work complements earlier microscopy studies of similar samples.[13,22] The goal is to understand how one can synthesize ceria and possibly other refractory oxide films, with large grains and well-defined (001) terminations.

II. EXPERIMENT

Cerium oxide films were deposited using a large-area pulsed laser deposition system. The films were deposited on *r*-cut sapphire and (001) YSZ at two substrate temperatures, 700 and 650 °C. The system was equipped with a KrF excimer laser source (248 nm wavelength, Lambda Physik Compex LPX 305i) operated at a repetition rate of 10 Hz and pulse energy of 600 mJ, which yielded an average deposition rate of ~0.5 nm/min. The processing atmosphere consisted of 175 mTorr partial pressure of oxygen. After deposition the samples were annealed in air at 1050 °C for periods of time ranging from 10 min to 2 h.[17] The sample surface roughness was analyzed by atomic force microscopy (AFM) in ambient atmosphere using Asylum Research MFP-3D-BIO atomic force microscope.

X-ray reciprocal-space mapping was chosen as a primary method for determining the lateral structure of these films. Figure 1 shows approximate locations of the reflections used in this work with respect to the film surface and directions of three principal scans: 2θ, ϕ, and ω. Each reflection is a three-dimensional object occupying a part of reciprocal space centered at the location given by the Bragg diffraction condition $|\mathbf{S}|=2\sin(\theta)/\lambda$, where θ is the reflection Bragg scattering vector $\mathbf{S}$ pointing at the reflection maximum. The reciprocal-space mapping can be described as sectioning of a three-dimensional reflection by a plane in reciprocal space. Two planes are commonly used for the purpose: 2θ-ω plane, normal to the film surface and containing $\mathbf{S}$ vector, and ϕ-ω plane, normal to the $\mathbf{S}$ vector, as shown in Fig. 1. During ϕ-ω or "pole figure" scan, a reflection is sectioned by the ϕ-ω plane; this provides information on the film texture. Combination of 2θ-ω scans and mapping the reflection in 2θ-ω plane allow separating normal and lateral strain and size broadening effects. In this work we present maps which are sections of ceria reflections by 2θ-ω plane.

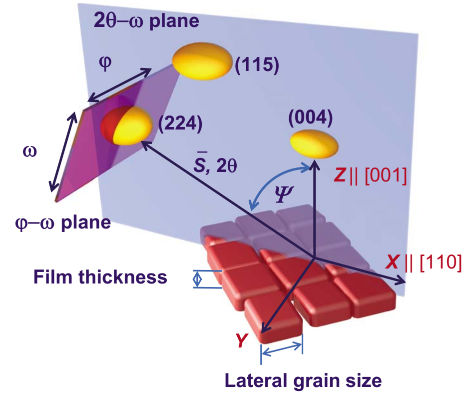

FIG. 1. (Color online) Schematic view of the x-ray reciprocal mapping geometry, showing the scattering vector S, the coordinate axes, and directions of the principal scans: ϕ, ω, and 2θ. Three reflections (004), (115), and (224), shown as ellipsoids, were mapped in a plane defined by [001] and [110] directions. The maps presented in this work are sections of a reflection by 2θ-ω plane. The lateral grain size and the film thickness are shown as the major contributors to the reflection broadening.

In an epitaxial (00*l*) ceria film only (002) and (004) peaks can be accessed in the symmetric scattering geometry, i.e., when the scattering vector $\mathbf{S}$ is normal to the film surface. More information can be accessed from mapping asymmetric (*hkl*) reflections with the $\mathbf{S}$ vector tilted at an angle ψ with respect to the film normal (Fig. 1). These reflections are important since the scattering vector $\mathbf{S}$ has nonzero lateral component S_x, thus providing insight on the lateral strain of the film. We have selected three reflections with significantly different inclination angles: (002), $\psi=0°$; (004) $\psi=0°$; (115), $\psi=15.4°$; and (224), $\psi=35.5°$. Mapping these reflections gives a relatively complete picture of the average film structure in both lateral and normal directions. Additionally, during the scans both incident and reflected beams stay in a plane defined by [001] and [110] directions. The constant instrument geometry with no in-plane rotation allows for quantitative comparison of maps of different reflections and assures that the instrument function stays constant. In the following we denote the $\mathbf{X}$ direction as one parallel to [110] of the CeO_2 layer and the $\mathbf{Z}$ direction as one parallel to [001]. Figure 1 also shows two sources of the reflection broadening: the film thickness and the lateral grain size were responsible for the reflections broadening in the $\mathbf{Z}$ and $\mathbf{X}$ directions, respectively.

Two film samples studied in this work were deposited on miscut *r*-cut sapphire substrates. The substrates were miscut at angles 2.2° and 5.4° with respect to $(1\underline{2}10)$ direction, so

that the direction of the slope coincided with the [110] direction of the CeO_2 film. The samples had in-plane anisotropy characterized by the azimuth angle Φ, $\Phi=0°$ corresponding to the S_x projection parallel to the slope of the miscut. For these samples two kinds of maps were recorded, one for $\Phi=0°$ (along the miscut direction) another for $\Phi=90°$ (across the miscut direction).

Reciprocal-space maps (RSMs) were recorded by a Rigaku Ultima III x-ray diffractometer equipped with parallel beam x-ray optics.[23] Parallel beam optics are capable of delivering high-intensity x-ray beams with low divergence, which is critical for mapping asymmetric (*hkl*) reflections. The x-ray mirror provided a high-intensity beam with 0.05° divergence; the divergence slit was set at 3 mm to achieve full sample illumination at the lowest x-ray source elevation angle [8.9° for (224) reflection]; the antiscatter and receiving slit were set to 0.5 and 0.25 mm, respectively. This configuration enabled constant resolution and the scattering vector inclination angle up to 80°. The instrument resolution in the **Y** direction (normal to 2θ-ω plane) was limited by acceptance of a vertical Soller slit, 0.5° in this experiment. Thus due to low in-plane resolution the recorded intensity was effectively integrated in the **Y** direction, which is a typical situation for a horizontal-slit diffractometer. The mapping was performed as a series of ω scans at various 2θ-ω angles. In this geometry the angular resolution of the ω scan was limited by the beam divergence and the slit geometry, 0.05°, thus remaining independent of 2θ angle. To achieve high intensity and useful count rate, especially for weak (115) and (224) reflections, we did not use a monochromator in the incident beam path. A simple estimate shows that the extra line broadening caused by unfiltered $K\alpha_2$ line for a CeO_2 (224) reflection ($|\mathbf{S}|=9.1$ nm^{-1}) would be 0.023 nm^{-1}. Given an average domain size of 20–30 nm for our film samples, $K\alpha_2$ line would introduce a significant error in strain and domain size analysis. Figure 2(A) illustrates the effect of unfiltered $K\alpha_2$ radiation on a RSM of the (224) reflection of 20 nm CeO_2 film on *r*-cut sapphire. The $K\alpha_2$ line contribution can be seen as stretching of the central Bragg peak in the 2θ-ω direction; this effect is known as the spectral spread of a reciprocal-space map.

Because the $K\alpha_2$ broadening is comparable to or less than the physical line broadening in these samples, a software deconvolution could be effectively applied to eliminate $K\alpha_2$ contribution to the reciprocal map profile.[24] Dedicated software utilizing a fast Fourier transform algorithm has been developed in the MATLAB interpreter. The program dissected the map into a series of 2θ-ω scans and the deconvolution procedure was applied to each scan using the instrument function consisting of two Lorentzians with 0.05° width at wavelength corresponding to $K\alpha_1$ and $K\alpha_2$ lines, $K\alpha_2$ being 50% of $K\alpha_1$ intensity. Finally the deconvoluted map was reassembled from the individual scans. Figure 2(B) illustrates the result of the deconvolution procedure applied to the raw map of a (224) reflection shown in Fig. 2(A). After the deconvolution procedure has been applied, the $K\alpha_2$ contribution is suppressed below 1% of the absolute peak intensity, as indicated by the disappearance of the Bragg peak distortion in the deconvoluted map [Fig. 2(B)]. The 2θ-ω resolution of the method was determined to be 0.07° by recording the spectrum of CeO_2 powder annealed for 10 h at 1000 °C in air and applying the deconvolution algorithm. The combination of parallel beam optics and $K\alpha_2$ deconvolution allowed for fast mapping of even relatively weak reflections; on average it took 1.5 h to record a map with 0.01 nm^{-1} resolution at ≈0.2% noise level.

A typical map of an (*hkl*) reflection can be approximated by an ellipse with the main axis inclined at an angle ζ with respect to S_x direction. Fewster[25] identified several factors that contribute to inclination and shape of an (*hkl*) map of an epitaxial film: domain size, microscopic tilt, and nonuniform strain. In a small-grained well-oriented thin film sample, where only domain size broadening is present, the (224) map would appear as a horizontal ellipse, $\zeta=0°$, with the normal and the lateral diameters of the ellipse being inversely proportional to the film thickness and the average lateral grain size, respectively. In the other extreme case of a large grain with large microscopic tilt, the map can be approximated as a narrow ellipse tilted with respect to S_x at $\zeta=\psi=35.2°$, the major diameter of the ellipse being approximately equal to $|\mathbf{S}|\delta\omega$, where $\delta\omega$ is the microscopic out-of-plane tilt of the film. In all the intermediate cases, when both the microscopic tilt and the domain broadening are equally contributing, a simple geometric argument allows separation of the contributions. Figure 2(B) schematically shows how normal ΔS_z^{-1} and lateral ΔS_z^{-1} integral widths of the reflection were determined from a three-dimensional Bragg peak profile. In the profile fitting algorithm used in this work the reflection profile was approximated as an inclined ellipse with profile cross sections along 2θ-ω and ω directions approximated by pseudo-Voigt functions. Both normal and integral half widths were determined from the approximation of the profile.

The same machine was used for x-ray reflectivity (XRR) measurements. A smaller divergence slit, 0.05 mm, has been set to minimize intensity variation at low-angle range. After the small-angle correction was applied the XRR profile was analyzed by the MOTOFIT software package.[26] The sample was modeled as a constant-density film on top of a substrate with the density equal to the theoretical value. The film thickness, film density, surface, and substrate-film roughness were the fitting parameters. The software performed the least-squares regression to extract the roughness and the density information from the XRR traces.

III. RESULTS

A. Reciprocal-space mapping of 20 nm ceria films on (001) YSZ and *r*-cut sapphire substrates

Figure 3 demonstrates the evolution of deconvoluted RSMs for two extreme cases: (i) a large-grained sample, 20-nm-thick ceria film on *r*-cut sapphire, deposited at 700 °C [Fig. 3(A)] and annealed for 1 h at 1050 °C [Fig. 3(B)]; (ii) a small-grained sample, 20-nm-thick ceria film, deposited at 650 °C on (001) YSZ [Fig. 3(C)] and annealed for 1 h at 1050 °C [Fig. 3(D)]. The maps are aligned vertically from the symmetric (004) reflection with zero inclination angle followed by skewed (115) $\psi=15.4°$ and (224) $\psi=34.5°$ reflections. A film deposited at 700 °C on *r*-cut sapphire has a fairly large initial grain size, as indicated by the narrow res-

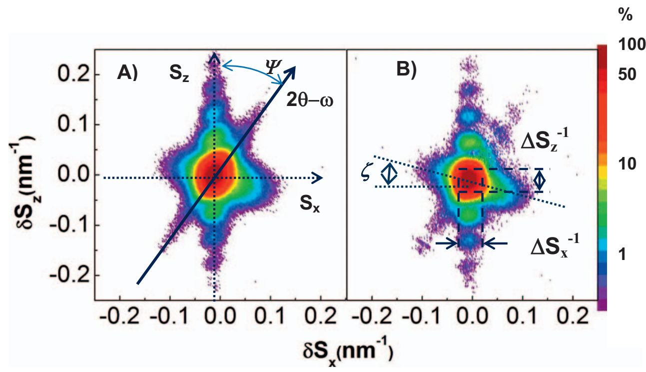

FIG. 2. (Color) Result of the $K\alpha_2$ deconvolution of a raw reciprocal-space map of a (224) CeO_2 reflection [panel (A)]. The deconvolution eliminates contribution of $K\alpha_2$ line, which is responsible for elongation of the map along 2θ-ω direction, indicated by a solid arrow in panel (A). This artifact is easily noticeable in the raw map [panel (A)] and is reduced by a factor of 10 in the deconvoluted map [panel (B)]. The logarithm of the normalized intensity (in %) was mapped according to the color scale bar on the right. Panel (B) schematically shows how lateral ΔS_x and normal ΔS_z integral broadening values were determined from the map and defines angle of inclination of the reflection ellipse ζ.

olution limited (004) reflection [Fig. 3(A)], however the Bragg peak is surrounded by a diffuse scattering tail. Upon examining the maps we notice that Bragg peaks become broader as we move from the symmetric (004) reflection with S_x=0 nm^{-1} to reflections with nonzero S_x, (115) and (224). On the other hand, the Bragg peak width in the **Z** direction remains practically unchanged for all the three maps. Figure 3(B) shows the effect of 1 h annealing at 1050 °C in air on the same set of RSMs. In these samples the RSM shape is dominated by lateral inhomogeneous (rms) strain which causes lateral broadening of tilted reflections (115) and (224) with nonzero lateral scattering vector component S_x. The normal direction broadening stayed constant as S_z changed, indicating the low normal strain of the film, as shown by dotted lines in Fig. 3(B).

Figures 3(C) and 3(D) reflect change in the microstructure of the 20 nm CeO_2 film deposited at 650 °C on (001) YSZ substrate. This figure is an illustration of a map set for a very small-grained sample: the as-deposited sample has columnar grain morphology with the lateral grain size smaller than the film thickness, which is indicated by the elliptical shape of the maps. By measuring the integral half-width of the Bragg reflection one can easily infer from maps in Fig. 3(C) that the as-deposited sample was comprised of 20-nm-long and 10-nm-wide columnar grains. After the annealing we observed lateral grain growth and reduction in the lateral rms strain, as demonstrated by narrower lateral reflections of the annealed sample [Fig. 3(D)], the lateral grain size approximately doubled after 1 h annealing. Due to proximity of very strong YSZ substrate reflections, the (004) and (224) maps contained a trace of the YSZ peak visible as a rod in the upper half of the map. This is a typical situation we encountered in CeO_2 on YSZ system: the grain growth saturated after approximately doubling the initial grain size.

Bulk ceria has a cubic structure, however the lattice mismatch and difference in the thermal expansion coefficient

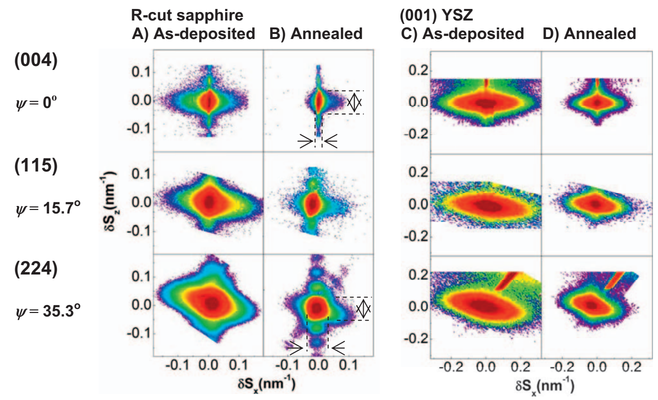

FIG. 3. (Color) Reciprocal-space maps of (004), (115), and (224) reflections of a 20 nm (001)-oriented CeO2 film on *r*-cut sapphire and (001) YSZ: (A) as deposited at 700 °C on *r*-cut sapphire, (B) after 1 h annealing at 1050 °C, (C) as deposited at 650 °C on (001) YSZ, and (D) after 1 h annealing at 1050 °C. Reduction in lateral strainlike disorder broadening and diffuse scattering by the annealing is clearly evident by comparing (224) maps in panels (A) and (B). Here ψ is the angle of inclination of the scattering vector S with respect to the film normal. Dotted lines in panel (B) show normal and lateral reflection widths in (004) and (224) reflections. Note that the normal width stays the same, while the lateral width significantly changes.

between the film and substrate introduce tetragonal distortion which is detected as a difference between the lattice parameters in the directions parallel to (a_p) and normal to (a_n) the substrate face. As a result of the film-substrate interaction, the film can be either coherently strained (mesomorphic) or relaxed. In a mesomorphic film the lateral lattice constant is equal to that of the substrate, while in a relaxed or partially relaxed film it is close to the bulk value. We derived both lateral and normal lattice constants from the spacings of

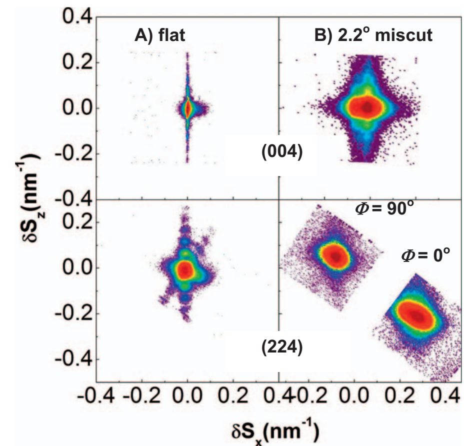

FIG. 4. (Color) Reciprocal-space maps of (004) and (224) reflections of 20 nm CeO_2 films deposited on a flat *r*-cut sapphire [panel (A)] and on 2.2° miscut substrate [panel (B)]. After the deposition at 700 °C both samples were annealed for 1 h at 1050 °C in air. For the miscut sample maps of (224) reflection both along (Φ =0°) and across (Φ=90°) the cut slope are presented. Note significant lateral broadening of both the (004) and (224) reflections of the miscut sample, especially in the Φ=0° direction.

(004) and (224) planes assuming a tetragonal distortion of the cubic lattice. Both lattice constants did not change during the annealing; the seven average values determined for seven samples of CeO_2 on sapphire were $a_p = 0.5439 \pm 0.0007$ nm, $a_n = 0.5400 \pm 0.0002$ nm; for seven samples of CeO_2 on (001) YSZ, $a_p = 0.5432 \pm 0.0005$ nm, $a_n = 0.5404 \pm 0.0002$ nm. The normal direction lattice constant is close to the bulk value, 0.541 134 nm; there is however a detectable tetragonal deformation that can be described as tensile strain, approximately 0.5%. Similarity in sign and value deformation was observed by Chen *et al.*[27] who studied structure of ceria films on YSZ-buffered Si. Close values of normal and lateral lattice constants suggest that these films are partially relaxed since the lateral strain, 0.5%, is much less than the misfit value of 5–10 %. High-resolution transmission electron microscopy (TEM) analysis of film-substrate interface in similar epitaxial ceria on (001) YSZ[28,29] films demonstrated that misfit strain in those samples was relieved by formation of misfit dislocations with Burgers vector $b = \frac{1}{2}[010]$, the dislocations being approximately 5 nm apart.

Other film samples deposited on practically flat (miscut $<0.1°$) substrates fall between the two extreme cases of small- and large-grained samples such as shown in Fig. 3. Ceria epitaxy exhibited quite different behavior on vicinally miscut surfaces. Figure 4 compares RSMs for (004) and (224) reflections for 20 nm film deposited on a flat substrate and a 2.2° miscut substrate after 1 h of annealing at 1050 °C. For the miscut sample (224) the map was recorded in two directions: along, $\Phi = 0°$, and across, $\Phi = 90°$, the cut slope. We conclude from Fig. 4 that the lateral grain growth is suppressed by the miscut, particularly in the direction along the miscut slope. The grains appear to be extended in the direction across the miscut slope, acquiring in-plane anisotropy. Significant microscopic tilt of ceria grains in the direction along the slope ($\Phi = 0°$) can be inferred from high inclination (30°) of the (224) map. Thus, even a miscut as small as 2.2° substantially degrades the film quality by preventing lateral grain growth and structure improvement by the isothermal annealing.

B. Evolution of the surface morphology during isothermal annealing

AFM and XRR were used to obtain information on local (AFM) and average (XRR) roughness of these films. XRRs characterize both surface and film-substrate interface roughness. The XRR trace is described by two parts: an angle-independent part up to the critical angle (for ceria ≈0.7°), followed by a rapid decay of the reflected wave intensity with superimposed thickness oscillations. The critical angle value allows the determination of the film density, while the decaying part contains information on the film surface and film-substrate interface roughness: higher critical angle corresponds to a denser film and slower reflectivity decay corresponds to lower roughness. Figure 5 shows the change in the XRR trace brought about by the annealing of the film (A) on *r*-cut sapphire deposited at 700 °C and (B) on (001) YSZ deposited at 650 °C; these are the same samples used in the

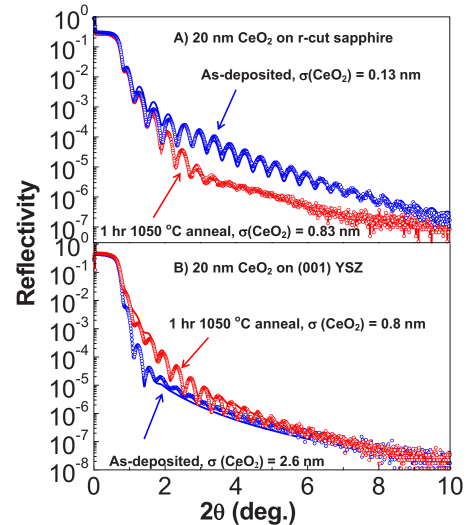

FIG. 5. (Color online) (A) Evolution of x-ray reflectivity profile after 1 h annealing at 1050 °C. X-ray reflectivity from as-deposited and annealed CeO_2 films (reciprocal maps of these samples are shown in Fig. 3). Solid line is the dynamic theory approximation assuming 20 nm CeO_2 layer on either Al_2O_3 [panel (A)] or YSZ substrate [panel (B)].

mapping experiment (Fig. 3). The film as deposited on *r*-cut sapphire consisted of very large strained grains with smooth surface; XRR trace gives very low roughness values of 0.13 nm. According to Fig. 3(B) after the annealing the strain relaxed; this also increased the film roughness to 0.83 nm possibly due to formation of grain facets. Film deposited on YSZ at 650 °C showed an opposite trend. The as-deposited sample had very high roughness, 2.6 nm; according to AFM, high roughness resulted from the very small-grain size and associated (111) faceting of grains, which also correlated with 10 nm lateral coherence length obtained from RSM shown in Fig. 3(D). AFM profiles show that after annealing the roughness improved due to lateral grain growth and formation of flat (001) terminations, which however are smaller than those of the film on *r*-cut sapphire.

Table I provides a brief summary of grain size and surface roughness derived from x-ray diffraction and AFM profiles. Atomic force microscopy data for the grain size are provided only for samples with well-defined terminations. Additionally, ceria density was calculated from the XRR critical angle. The density values of as-deposited and annealed films obtained from XRR measurements are equal (within 2% experimental error for the diffractometer used in this work) to the bulk density of ceria density value of 7.13 g/cm^3. We did not observe statistically significant density change after the annealing.

One can notice from Table I that deposition at 650 °C produces equally small-grained samples, 10 nm lateral grain diameter, on both *r*-cut sapphire and (001) YSZ substrates. These samples respond quite differently to the annealing after 1 h of annealing at 1050 °C ceria on *r*-cut sapphire has a lateral grain size approximately four times larger than the film on (001) YSZ. To understand the mechanism of the grain growth we have to examine both AFM and x-ray diffraction data in greater detail. AFM profiles shown in Fig. 6

TABLE I. The surface roughness and the film density determined from XRR profiles; lateral domain size obtained from reciprocal-space maps and AFM profiles. The density was calculated from the critical angle values of XRR profiles.

Substrate	r-cut sapphire				YSZ			
Deposition temperature T_D (°C)	650		700		650		700	
Annealing time t_A (min)	0	60	0	60	0	60	0	60
XRR density ρ (g/cm^3)	7.1	6.9	7.0	7.2	7.2	6.9	6.9	7.1
XRR roughness σ (nm)	3.3	0.82	0.13	0.83	2.6	0.8	0.25	0.18
Lateral domain ξ_x (nm)	11.1	95.7	60.0	105.0	10.5	25.3	19.4	44.8
AFM grain size d_x (nm)	19	240			18			

compares effect of isothermal annealing at 1050 °C for 1 h on the AFM profiles of 20 nm ceria films deposited on r-cut sapphire [panel (A)] and (001) YSZ [panel (B)]. Additionally, ω scans of these samples after the deposition and after 10 and 60 min of annealing are provided for comparison.

Figure 6 provides the evidence that even if the average initial grain size in these samples is almost the same, the grain-size distribution is quite different and it is this parameter which is most likely responsible for the difference in the growth mode. Side by side comparison of surface morphology of 20 nm films on r-cut sapphire [Fig. 6(A)] and YSZ [Fig. 6(B)] shows that the film on r-cut sapphire contains a small number of abnormally large grains, while ceria on YSZ exhibits mostly monomodal grain-size distribution. Transverse (ω) scans of (004) reflection of as-deposited films offers no evidence of bimodal grain population. However, after 10 min of annealing ω scan of ceria on r-cut sapphire becomes distinctly bimodal, while YSZ sample stays monomodal. Indeed, the ω scan of (004) reflection of YSZ sample can be approximated by a single-width pseudo-Voigt function with the coefficient of determination $R^2=0.99$. A single-width pseudo-Voigt function can only approximate the ω scan of the sapphire sample to the level of $R^2=0.97$. To achieve a value of 0.99 we have to implement a two-curve approximation, one with $\delta\omega=0.2°$ and another with $\delta\omega=0.78°$. This suggests existence of at least two grain populations with the average grain sizes of 54 and 13 nm, smaller grains being slightly misaligned with respect to the larger ones.

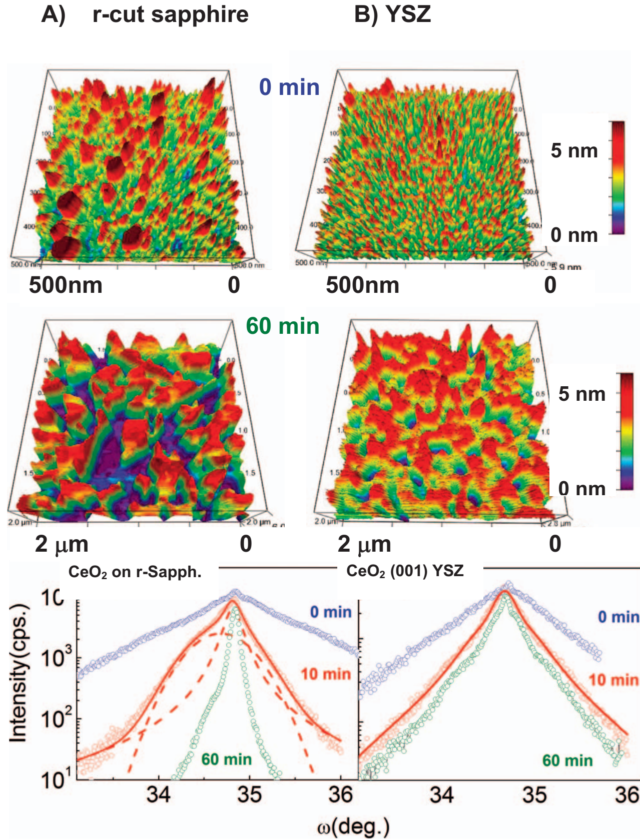

FIG. 6. (Color) Effect of annealing at 1050 °C for 1 h on AFM profiles of 20 nm CeO_2 films on r-cut sapphire [panel (A), left] and (001) YSZ [panel (B)]. Note the lateral scale difference between the upper and bottom AFM profiles. The bottom panel shows corresponding ω scans of the (004) reflection. The solid lines are pseudo-Voigt approximations. For the ceria on r-cut sapphire sample [panel (A)], the best fit is a two-component curve, which is the evidence of a bimodal grain-size distribution. Grain-size distribution in the ceria on YSZ sample [panel (B)] is well described by a monomodal approximation.

Finally, after 1 h annealing, large faceted grains with flat tops appear on the surface of the sample deposited on r-cut sapphire, with the average facet height of 3 nm. Development of a large-grain structure after 1 h annealing causes sharpening of ω scan of the sample [Fig. 6(A)]. The lateral coherence length of 95 nm, determined from RSM, correlates with the apparent grain size in Fig. 6(A), indicating that large grains are indeed single crystals. Surface features in the AFM profile [Fig. 6(B)] are much larger than the actual grain size obtained from the rms analysis. The AFM line profile of this sample shows mostly rounded surface terminations, indicating that 100–200 nm wide apparent "grains" in the lower AFM profile [Fig. 6(B)] are actually conglomerates of much smaller subgrains.

IV. ANALYSIS OF THE LATERAL STRUCTURE

In the reciprocal mapping experiment we measure the intensity of the scattered x-ray radiation in the vicinity of Bragg reflections. We will use kinetic approximation, which is justified for small-grain (<100 nm) samples. For a crystallite comprised of atoms with scattering factor f, with structural distortion characterized by the displacement field

$u(x,y,z)$ the profile of scattered intensity in reciprocal space is given by the following equation:

$$I(S) = \sum_m \sum_n f_n f_m \exp\{-2\pi i S \cdot (r_n - r_m)\} \times \exp\{-2\pi i S \cdot (u_n - u_m)\}, \quad (1)$$

where **S** is the scattering vector. Reciprocal-space maps, like shown in Fig. 3, are sections of the three-dimensional intensity $I(\mathbf{S})$ profile by a plane.

For an infinite undistorted ($u=0$) crystal Eq. (1) predicts resolution-limited Bragg peaks when the Laue conditions are satisfied. According to the classic analysis by Krivoglaz,[30] the effect of structure defects on the diffraction pattern of an infinite crystal depends on how fast the displacement field u decays as a function of distance from the defect. Small defects with a fast decay of the displacement field (type-I defects), for example, point vacancies with $u \propto 1/r^2$, introduce diffuse scattering halo around the Bragg peak. Type-II defects with slow decay of the displacement field, for example, dislocations with $u \propto 1/r$, affect the peak shape. Dislocations breaks an ordered crystal into subgrains, thus introducing rotational and strain broadening of Bragg reflection profiles.[31]

If the sample is comprised of small grains, the experimentally measured $I(\mathbf{S})$ is a sum of incoherent contributions of the crystallites. As shown by Guinier,[32] if the crystallites are free of disorder ($u=0$), the RSMs of all the reflections would be identical two-dimensional Fourier transforms of the average crystallite shape. Hence the RSM of a real object would be a convolution of an unknown shape factor and also unknown displacement field, produced primarily by type-II defects. The problem can be simplified by assuming that $(u_n - u_m)$ term in Eq. (1) is a Gaussian random variable which depends on the relative coordinates $r_m - r_n$.[33,34] In the limit of small displacements broadening of $(00l)$ Bragg peak induced by type-II defects in direction j (in our case j is either x or z) would be proportional to the following product: $S_z \langle \varepsilon_{jz}^2 \rangle^{1/2}$, where

$$\langle \varepsilon_{ji}^2 \rangle = \left\langle \left[\frac{\partial u_i(r_j)}{\partial r_j} \right]^2 \right\rangle . \quad (2)$$

Here $\langle \varepsilon_{ji}^2 \rangle^{1/2}$ (in the following we use a simplified notation ε_{ji}) is commonly referred to as rms strain tensor. For a polycrystalline material Eq. (2) yields the well-known Williamson-Hall strain broadening formula.[35] More exact treatment of dislocation-induced broadening in polycrystalline materials, so-called modified Williamson-Hall method, suggested by Ungar *et al.*,[36,37] takes into account actual dislocation slip system thus accounting for anisotropic broadening of (hkl) reflections and allowing for better determination of domain size and dislocation density. An oriented material subjected to anisotropic strain broadening of $(00l)$ reflection in normal direction (z or 2θ-ω scan) is affected by the ε_{zz} strain component, and the influence of the off-diagonal term ε_{zx} can be detected by measuring width of the ω scan.[38] Predicting shape of a reflection in such a material requires a model of type-II defects, responsible for the strain broadening. The following discussion is based on an assumption that the strain field in these samples is generated by threading edge dislocations. For the pure edge type dislocation the rms strain angular dependence was derived by Hordon and Averbach,[39]

$$\langle \varepsilon(\Delta,\gamma)^2 \rangle = \left[\frac{5b^2}{64\pi^2 r^2} \right] \ln\left(\frac{r}{r_0} \right) (2.45 \cos^2 \Delta + 0.45 \cos^2 \gamma), \quad (3)$$

where Δ is the angle between the dislocation glide plane normal and $[hkl]$, γ is the angle between the dislocation Burgers vector and $[hkl]$, r_0 is the dislocation core radius, and r is the upper limit for integration of the strain field in the radial direction from the dislocation core. Equation (3) predicts that rms strain generated by pure edge dislocations would weakly affect reflections from planes normal to the slip plane but would contribute more strongly to broadening of reflections originating from (hkl) planes less tilted with respect to the slip plane. Results of studies of $Fm3m$ (calcium fluorite structure) symmetry compounds[40] along with TEM data on ceria films[28,29] indicate that $\langle 011 \rangle$ $\{001\}$ is the principal glide system in $Fm3m$ materials. We note, from Fig. 3(B), that in our samples the normal rms strain component ε_{zz} is much less than the lateral one ε_{xx}: there is noticeable lateral broadening for reflections with large lateral scattering vector component, at the same time normal broadening stays unchanged. We interpret this observation as strain broadening by edge dislocations with $\{100\}$ set of glide planes. Such a dislocation arrangement would influence symmetric $(00l)$ reflections only through relatively weak $\cos^2 \gamma$ term in Eq. (3); at the same time width of asymmetric (hkl) reflections with nonzero Δ angle would be affected by a stronger $\cos^2 \Delta$ term. Equation (3) describes strain field of an isolated dislocation. X-ray diffraction detects the net field strain field originating from an ensemble of dislocations. In our case an array of parallel edge dislocations would produce the strain field with the orientation term predicted by Eq. (3), however, dependence of the net rms strain magnitude on the dislocation density may strongly depend on the details of the dislocation arrangement.[41]

In the following analysis we assume that broadening of an (hkl) reflection in direction I, ΔSi, is a sum of shape term $1/\xi_i$ and the strain term proportional to $4\varepsilon_{ii}S_i$, i being either x or z, ξ_i is the average domain size in the direction i, $S_x = |\boldsymbol{S}| \cdot \sin(\psi)$, and $S_z = |\boldsymbol{S}| \cdot \cos(\psi)$, where ψ is the inclination angle (Fig. 2). This approach presumes that the normal component of the deformation field u_z is much less than the lateral one u_x, which is consistent with purely lateral strain. Figure 7 shows the resultant dependence of both lateral ΔS_x and normal ΔS_z broadening components, calculated from RSMs shown in Fig. 3 as a function of the scattering vector $\mathbf{S}$ projection on $\mathbf{X} \| [110]$ and $\mathbf{Z} \| [001]$ axes. All the four samples appear unstrained in the normal direction; the only source of the normal broadening is the finite scattering domain size $\xi_z = 23 \pm 2$ nm. This value agrees well with the projected film thickness, 20 nm, and the thickness determined from XRR measurements, 21 ± 0.5 nm. The most prominent difference between the samples is the lateral broadening, which has two characteristics: (i) lateral scatter-

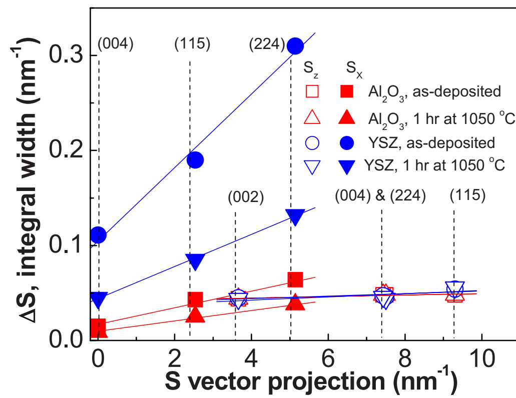

FIG. 7. (Color online) Williamson-Hall plot for normal peak broadening (Z component, open symbols) and lateral broadening (X component, closed symbols) of 20 nm ceria films deposited on r-cut sapphire and (001) YSZ. The anisotropic broadening information was obtained from reciprocal-space maps shown in Fig. 3; the data points are labeled by (hkl) indices of the corresponding reflections. The connecting lines are linear approximation fits.

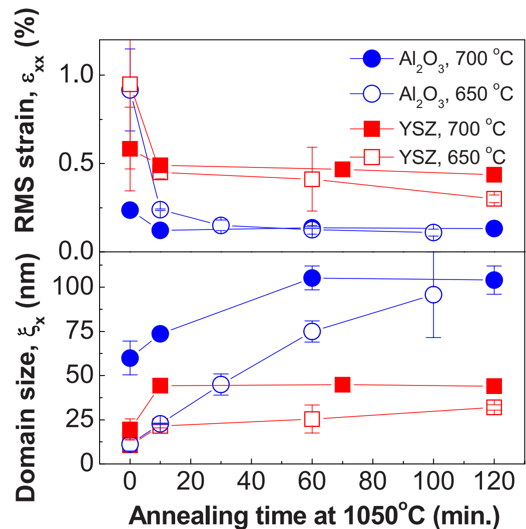

FIG. 8. (Color online) Evolution of the lateral domain size ξ_x and lateral rms strain ε_{xx} with annealing time. Note stagnation of grain growth in YSZ samples after 10 min of annealing.

ing domain size ξ_z determined as the intersection of $\Delta S_x(S_x)$ line with the Y axis (ii) and lateral rms strain ε_{xx} determined from a slope of this line. The films on YSZ substrate have very small lateral coherence length and high lateral strain. Annealing produces both lateral grain growth and rms strain reduction. The films on r-cut sapphire exhibit significantly better structure, which further improves upon annealing.

Figure 8 summarizes the line profile analysis as time evolution plots of the lateral domain size and rms strain for four sets of samples: 20 nm CeO_2 films on YSZ and r-cut sapphire deposited at 650 and 700 °C. Consistently, low deposition temperature produces smaller grains and high initial rms strain. However, after approximately 2 h of annealing films deposited on the same substrate converged toward a common structural state, which changed little upon further annealing. In the YSZ samples the grain growth saturated at approximately 30 nm lateral size with 0.5% residual strain, while the sapphire samples demonstrated much faster grain growth with lateral domain size exceeding 100 nm and low lateral rms strain value. We conclude from this that lateral grain growth is closely correlated with relaxation of the lateral rms strain. However, the process is strongly affected by the type of substrate. Surprisingly the YSZ substrate, which has better lattice match (5%) than r-cut sapphire (4% and 12%), exhibits slower grain growth and overall lower structural quality.

V. DISCUSSION

In this section we discuss two structural aspects of these samples: the initial grain size and strain in as-deposited samples and evolution of the grain structure and the strain during the thermal annealing. Initial granularity in epitaxial films is a consequence of Volmer-Weber growth mechanism.[42] During Volmer-Weber growth the epitaxial phase nucleates as three-dimensional islands which expand and coalesce into a continuous layer. This process is accompanied by significant changes in character of the elastic strain: the isolated islands are subjected to compressive strain, which is replaced by tensile strain as the islands make contact. The coalescence occurs spontaneously when the overall system energy can be reduced by joining adjacent sides of two growth islands into a grain boundary, as described by several models.[43–45] The spontaneous grain joining process, also known as "grain-boundary zipping," generates tensile strain. Thus a film with smaller initial grain size is expected to be more strained than a film with larger grains. Another source of elastic strain, specific to epitaxial structures, is caused by interaction between the substrate and the film material. According to van der Merwe theory,[46] the film-substrate interface produces strain due to the mismatch between the lattice constants of the films and the substrate material. The elastic strain in ceramic materials is rarely uniform; it tends to relax via plastic flow and generation of dislocations at the film-substrate interface and at the grain boundaries.[47,48] These dislocations produce oscillatory displacement of the lattice which can be detected as rms strain by x-ray diffraction.

Grain growth is one of the mechanisms capable of reducing energy stored in a film in the form of grain-boundary surface energy and elastic energy associated with the initial strain. The earliest model of grain growth in metals first proposed by Burke and Turnbull[49] treats the grain-boundary motion as being driven by pressure differential associated with the grain-boundary curvature. A kinetic equation based on this consideration predicts square-root dependence of the grain size on the postannealing time.[49] Study of grain-growth kinetics in $Ce_{0.8}Gd_{0.2}O_{1.9-x}$ ceramic (polycrystalline) films with <100 nm grains by Rupp *et al.*[50] demonstrated that in these samples curvature-driven Burke-Turnbull grain kinetics is only observed at temperature >1100 °C after the rms strain is completely relaxed. At this temperature the ceramic structure evolved in recovery-grain-growth sequence, typical for highly deformed materials.[51] At lower temperatures, the grain growth was observed to be consistent with grain-

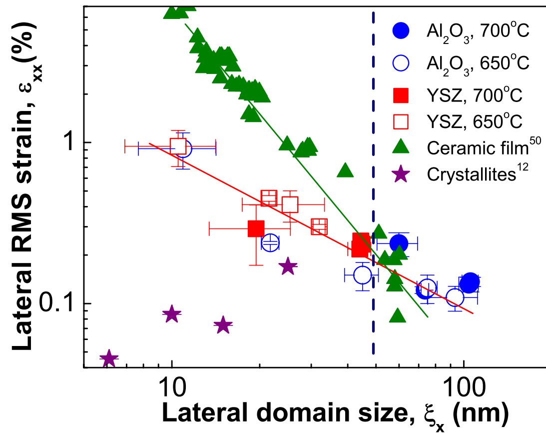

FIG. 9. (Color online) Correlation of the lateral coherence length ξ_x with the lateral rms strain ε_{xx}. The dashed vertical line is 2.5 thickness limit for the normal grain growth predicted by the Mullins thermal grooving model (Ref. 56). Note that ξ_x for YSZ sample is on the left side of the line. Filled triangles are data on ceramic films, digital data kindly provided by Rupp *et al.* (Ref. 50), and stars are data on isolated nanocrystals adapted from Zhang *et al.* (Ref. 12). For these data sets the rms strain and the grain-size values were derived from powder diffraction spectra. The solid lines are $\varepsilon \propto \xi^{-\alpha}$ fits, α=0.87±0.13 for the films and α=2.1±0.06 for the ceramic.

boundary diffusion and gradual rms strain relaxation. In these ceramic films the grain growth was limited to 50 nm, possibly due to solute drag effect and/or impurity accumulation at the grain boundary.

Close relationship between the grain size and the rms strain in our samples is demonstrated in Fig. 9, where we correlate the rms lateral strain with the lateral coherence length ξ_x using the data shown in Fig. 8. Data for nanograined $Ce_{0.8}Gd_{0.2}O_{1.9-x}$ ceramic films provided by Rupp[50] are also plotted as closed triangles; data on isolated nanocrystals adapted from work of Zhang *et al.*[12] are plotted as stars. Data for the ceramic and the nanocrystallites were calculated from powder diffraction spectra, thus representing an orientation average of the grain size and the rms strain. These sets of data can be classified as (i) a two-dimensional case of a film with columnar grains with free surface and vertical low-angle grain boundaries, (ii) a three-dimensional case of a ceramic film with interconnected high-angle grain boundaries, and (iii) the isolated unsupported ceria crystallites.

Isolated ceria crystallites are practically dislocation-free, as indicated by very low level of rms strain in these samples. Low dislocation content in submicron crystals is due to high surface area, which creates multiple routs for the dislocation escape and is often referred as "dislocation starvation" effect.[52] Both ceramic and film samples show high level of initial or "as grown" defects, which annihilate as the grain growth is initiated by the high-temperature annealing. The solid lines represent $\varepsilon \infty \xi^{-\alpha}$ fits, best fit exponent values being α=0.87±0.13 for the 20 nm ceria films and α=2.1±0.6 for the ceramic. The initial strain dependence on the grain size in thin films was explained by Seel and Thompson[53] who numerically modeled average lateral strain $\langle\varepsilon\rangle$ associated with the island zipping and found that $\langle\varepsilon\rangle \propto R^{-\alpha}$, where R is the average island radius and α is an exponent varying from 0.9 to 1.4, depending on the island-substrate contact angle. The same model predicts that the grain-boundary zipping would produce normal strain less than 5% of the lateral component, in agreement with the absence of ε_{zz} rms strain demonstrated in Fig. 7. We conclude from Figs. 7 and 9 that dependence of the initial rms strain on the lateral grain in as-deposited films can be accounted by dislocations generated by relaxation of elastic deformation of interconnected Volmer-Weber islands. This also implies that the defect structure of these samples is dominated by the grain coalescence rather than by the film-substrate interface.

During annealing we observe a natural process of strain relaxation and grain growth. We can use the Hordon-Averbach result [Eq. (3)] to clarify how defect annihilation is related to the grain growth. Omitting unessential factors in Eq. (3) and equating the upper integration limit r to the average distance between the dislocations h,[39] we obtain $\varepsilon \propto b/h$. If number of dislocations within a grain is N_d, $h=(R^2/N_d)^{1/2}$, where R is the grain diameter, hence $\varepsilon \propto bN_d^{1/2}/R$ if N_d stays constant $\varepsilon \propto 1/R$. The approximation for the 20 nm films in Fig. 9 can be interpreted as a combination of grain-size dependent initial strain and redistribution of a constant number of dislocations within the growing grains; the annihilation of dislocations seems to be taking place only in the collapsing grains. This model fails to explain faster relaxation of strain in ceramics, $\varepsilon \propto 1/R^2$. The important difference is that in a ceramic grain boundaries are mostly of the high-angle type, while in an epitaxial film all the grain boundaries are low-angle ones. High-angle boundaries generate higher strain, at the same time they are known to absorb dislocations far more readily than low-angle grain boundaries.[54,55] We attribute the difference in the relaxation behavior between the epitaxial films and the ceramics in Fig. 9 to higher dislocation absorption rate by high-angle grain boundaries.

Experimental uncertainties of grain-size time dependences shown in Fig. 8 do not allow us to rule out the Turnbull-Burke mechanism in favor of grain-boundary diffusion. We note, however, that the time evolution of grain size of ceria deposited on r-cut sapphire at 650 °C has extensive linear part, a clear deviation from the Turnbull-Burke prediction. This observation and the fact that films on r-cut sapphire grows to much larger lateral diameter than films on (001) YSZ suggest two qualitatively different growth mechanisms.

Summarizing the observations we can classify grain growth in ceria films on (001) YSZ as normal. The most distinct feature of normal grain growth is monomodal distribution of grain sizes. The grains expand uniformly until larger grains, with more than seven sides consume grains with fewer sides and start to impinge on each other.[57] Monomodal grain-size distribution in (001) YSZ samples is confirmed by AFM profiles and a high fidelity approximation of rocking curves by a single pseudo-Voigt function: an example is shown in Fig. 6(B). It is well known that normal grain growth in two dimensions is limited by the sample thickness: once the lateral grain size reaches two to three

times thickness of a film[58] or a sheet[59] the grain growth practically stops. It has been shown by Mullins[56,60] that this effect occurs due to pinning of the grain boundaries by thermal grooves developing at a later stage of grain growth. Qualitatively, the effect can be explained by slow kinetics of normal growth, which allows for appreciable surface mass transfer and groove formation. The 2.5× thickness limit is shown by a dotted line in Fig. 9, notably that all the (001) YSZ samples are on the left side of this line. Thermal grooving is well confirmed in oxide ceramics with micron-size grain boundaries;[61] however it is not clear whether rounded slopes on AFM profile in Fig. 6(B) can be interpreted as such. An alternative explanation would be grain-growth stagnation by solute drag or impurity buildup in grain boundaries. We note that grains in films on *r*-cut sapphire deposited under identical conditions well exceed the 2.5× thickness limit, strongly suggesting thermal grooving as the grain-growth limiting mechanism.

To understand how (001) CeO_2 grains on *r*-cut sapphire are capable of growing much larger than the same material on (001) YSZ given similar initial grain size we have to consider the possibility of abnormal grain growth. Abnormal or secondary grain growth activates when a small number of grains gain a small energetic or kinetic advantage over the rest of the grain population.[62] This type of grain growth is widely encountered in various systems, the important applications of the phenomenon are the formation of (110)[100] (Goss) texture in Fe-Si alloy[63] used as a core in modern transformers and (001)[100] texture in fcc metals, such as Ni,[64] which finds application as a substrate for superconducting tapes produced by cold rolling-recrystallization (RABiTS) process[65] and low-resistivity copper films.[66] Abnormal grain growth is supported by energy stored in small grains adjacent to the abnormal grain, therefore rate of this growth changes little over time.[57] In contrast normal grain growth stops once the growing grain depletes its stored energy. This allows abnormal grains to achieve extraordinary dimensions and avoid thermal grooving boundary pinning. Additionally, abnormal grains in metals are known to contain about ten times less threading dislocations than normal grains, giving abnormal grains an extra energetic advantage.[67,68]

Abnormal growth can be activated by a variety of conditions, such as initial grain-size fluctuations, grain-boundary energy anisotropy, mobility variations, and combinations of these factors.[62] In a thin film, substrate-film interface and free surface energy play significant roles in grain-growth kinetics. As pointed out by Frost *et al.*,[69] even a gain of several percent in the free surface energy would allow an abnormal grain to overcome the Mullins barrier and grow to a lateral dimension well over the 2.5× thickness limit. In a majority of metals the abnormal grains have favorable orientation compared to the rest of the population, thus being capable of rapid growth due to anisotropy of the grain-boundary energy. This mechanism seems unlikely in our case since 2θ and ω scans did not reveal presence of significant amount of texture other than (001). We suggest that the abnormal grains, present in the initial population, are much larger in addition to being possibly better oriented and less strained than the rest. This hypothesis is supported by correlating CeO_2 (004) ω scans with the surface morphology of the two films shown in Fig. 6(A). The average initial grain size determined from AFM profiles in Figs. 6(A) and 6(B) is almost identical; however the AFM profile of the sapphire sample in Fig. 6(A) clearly indicates grain-size fluctuations, some grains appearing larger than the others. After 10 min of processing, bimodal grain-size composition starts to show in ω scan as supported by the two-curve approximation in Fig. 6(A), whereas (001) YSZ sample stays monomodal throughout the processing. We do realize that bimodal rocking curves of epitaxial structures are known to have various origins, such as special dislocation structure,[34] diffuse scattering from pointlike defects,[70] and transition from large to small-grain structure in the upper portion of the film.[28] The following evidences support the bimodal scenario: (i) the ratio between amplitude of two approximation components stays the same as the reflection order increases from (002) to (004), thus making defect-induced mechanism unlikely; (ii) development of a sharp ω-scan component closely correlates with development of grainlike features on AFM profiles.

Not only type of substrate but also state of the substrate surface determines whether abnormal grain growth is activated. Figure 4 shows that 2.2° miscut of *r*-sapphire substrate effectively suppressed the abnormal growth. Both AFM and rocking curve analysis indicate that the initial grain distribution stayed uniform, consisting of elongated grains 13 nm wide and 30 nm long. The shortest-grain length corresponds to the terrace width of the miscut *r*-cut sapphire: at 2.2° miscut angle it is 14 nm. Most likely, higher roughness of the miscut substrate increases the nucleation density and prevents formation of large grains, which are essential for the initiation of the abnormal growth, at the same time normal growth is limited by the substrate terrace width, thus producing small grains.

VI. CONCLUSION

This work demonstrated the effective use of reciprocal-space mapping for quantitative analysis of grain-growth kinetics in (001)-oriented ceria films deposited on two types of substrates: (001) YSZ and *r*-cut sapphire. X-ray diffraction profiles of these samples are dominated by domain broadening and lateral rms strain originating from grain boundaries. The average lateral grain size was found to be inversely proportional to the lateral rms strain. After isothermal annealing, films on *r*-cut sapphire exhibited faster grain growth and better structural quality than identical films deposited on (001) YSZ. We ascribe the difference to the onset of abnormal grain growth, which arises due to large fluctuation of the initial grain size in the films on *r*-cut sapphire. The nonuniform grain-size distribution is corroborated by AFM surface profile and rocking curve analysis. The effect is suppressed by a 2.2° miscut due to monomodal grain-size distribution in a miscut sample. The result proves that abnormal grain growth can be utilized to achieve large terminations of high-energy oxide surfaces in very thin films. It still remains unclear how the substrate surface chemistry is related to the grain-size distribution. One possibility is large nanoscale fluctuations of cohesion energy between $(1\bar{2}10)$ sapphire and

ceria (001) surfaces, which leads to nonuniform nucleation. This hypothesis has to be confirmed by detailed surface analysis of various substrates.

ACKNOWLEDGMENTS

This paper has been authored by Brookhaven Science Associates, LLC under contract with the Office of Electricity Delivery and Energy Reliability, U.S. Department of Energy. Research was carried out in part at the Center for Functional Nanomaterials, Brookhaven National Laboratory, which is supported by the Office of Basic Energy Sciences, U.S. Department of Energy under Contract No. DE-AC02-98CH10886. We would like to thank Mas Suenaga, Arnie Moodenbaugh, Steven Shapiro, and David Welch from Brookhaven National Laboratory and Eliot Specht from Oak Ridge National Laboratory for helpful comments and suggestions. We greatly appreciate help from Jennifer Rupp, ETH Zurich, Switzerland for providing digital data used in this work.

---

*Author to whom correspondence should be addressed; solov@bnl.gov

[1] B. Skårman, L. R. Wallenberg, P.-O. Larsson, A. Andersson, J.-O. Bovin, S. N. Jacobsen, and U. Helmersson, J. Catal. **181**, 6 (1999).
[2] O. Costa-Nunes, R. J. Gorte, and J. M. Vohs, J. Power Sources **141**, 241 (2005).
[3] B. C. H. Steele and A. Heinzel, Nature (London) **414**, 345 (2001).
[4] V. F. Solovyov, Q. Li, H. Wiesmann, P. Oleynikov, and Y. Zhu, Supercond. Sci. Technol. **21**, 125013 (2008).
[5] M. Baudin, M. Wójcik, and K. Hermansson, Surf. Sci. **468**, 51 (2000).
[6] D. C. Sayle, T. X. T. Sayle, S. C. Parker, C. R. A. Catlow, and J. H. Harding, Phys. Rev. B **50**, 14498 (1994).
[7] G. S. Herman, Phys. Rev. B **59**, 14899 (1999).
[8] N. Cabrera, Surf. Sci. **2**, 320 (1964).
[9] C. Herring, Phys. Rev. **82**, 87 (1951).
[10] Z. L. Wang and X. Feng, J. Phys. Chem. B **107**, 13563 (2003).
[11] L. D. Marks, Surf. Sci. **150**, 358 (1985).
[12] F. Zhang, Q. Jin, and S.-W. Chan, J. Appl. Phys. **95**, 4319 (2004).
[13] S. N. Jacobsen, U. Helmersson, R. Erlandsson, B. Skarman, and L. R. Wallenberg, Surf. Sci. **429**, 22 (1999).
[14] F. Wu, A. Pavlovska, D. J. Smith, R. J. Culbertson, B. J. Wilkens, and E. Bauer, Thin Solid Films **516**, 4908 (2008).
[15] J. A. Thornton, Annu. Rev. Mater. Sci. **7**, 239 (1977).
[16] A. G. Zaitsev, G. Ockenfuss, D. Guggi, R. Wordenweber, and U. Kruger, J. Appl. Phys. **81**, 3069 (1997).
[17] K. Develos-Bagarinao, H. Yamasaki, Y. Nakagawa, J. C. Nie, M. Sohma, and T. Kumagai, Nanotechnology **18**, 165605 (2007).
[18] M. Becht, F. Wang, J. G. Wen, and T. Morishita, J. Cryst. Growth **170**, 799 (1997).
[19] M. Patel, K. Kim, M. Ivill, J. D. Budai, and D. P. Norton, Thin Solid Films **468**, 1 (2004).
[20] N. Savvides, A. Thorley, S. Gnanarajan, and A. Katsaros, Thin Solid Films **388**, 177 (2001).
[21] S. Chromik, M. Cannaerts, S. Gazi, C. Van Haesendonck, M. Spanková, P. Kús, and S. Benacka, Physica C **371**, 301 (2002).
[22] M. Spanková, I. Vávra, S. Gazi, D. Machajdík, S. Chromik, K. Fröhlich, L. Hellemans, and S. Benacka, J. Cryst. Growth **218**, 287 (2000).
[23] L. Jiang, B. Verman, B. Kim, Y. Platonov, Z. Al-mosheky, R. Smith, and N. Grupido, Rigaku J. **18**, 13 (2001).
[24] P. A. Janssen, *Deconvolution with Application in Spectroscopy* (Academic, New York, 1984).
[25] P. F. Fewster, Rep. Prog. Phys. **59**, 1339 (1996).
[26] A. Nelson, J. Appl. Crystallogr. **39**, 273 (2006).
[27] C.-H. Chen, A. Saiki, N. Wakiya, K. Shinozaki, and N. Mizutani, J. Cryst. Growth **219**, 253 (2000).
[28] A. Cavallaro, F. Sandiumenge, J. Gàzquez, T. Puig, X. Obradors, J. Arbiol, and H. C. Freyhardt, Adv. Funct. Mater. **16**, 1363 (2006).
[29] C. M. Wang, S. Thevuthasan, and C. H. F. Peden, J. Am. Ceram. Soc. **86**, 363 (2003).
[30] M. A. Krivoglaz, *Theory of X-ray and Thermal Neutron Scattering by Real Crystals* (Plenum, New York, 1969).
[31] J. E. Ayers, J. Cryst. Growth **135**, 71 (1994).
[32] A. Guinier, *X-ray Diffraction in Crystal, Imperfect Crystals and Amorphous Bodies* (Freeman, San Francisco, London, 1963).
[33] S. K. Sinha, E. B. Sirota, S. Garoff, and H. B. Stanley, Phys. Rev. B **38**, 2297 (1988).
[34] P. F. Miceli and C. J. Palmstrom, Phys. Rev. B **51**, 5506 (1995).
[35] B. E. Warren, *X-ray Diffraction* (Addison-Wesley, New York, 1969).
[36] T. Ungar and A. Borbely, Appl. Phys. Lett. **69**, 3173 (1996).
[37] T. Ungár, I. Dragomir-Cernatescu, D. Louër, and N. Audebrand, J. Phys. Chem. Solids **62**, 1935 (2001).
[38] A. Boulle, R. Guinebretiere, and A. Dauger, J. Phys. D **38**, 3907 (2005).
[39] M. J. Hordon and B. L. Averbach, Acta Metall. **9**, 237 (1961).
[40] H. Zogg, S. Blunier, A. Fach, C. Maissen, P. Müller, S. Teodoropol, V. Meyer, G. Kostorz, A. Dommann, and T. Richmond, Phys. Rev. B **50**, 10801 (1994).
[41] T. Ungár, Mater. Sci. Eng., A **309-310**, 14 (2001).
[42] B. Lewis and J. C. Anderson, *Nucleation and Growth of Thin Films* (Academic Press, New York, 1978).
[43] J. A. Floro, E. Chason, R. C. Cammarata, and D. J. Srolovitz, MRS Bull. **27**, 19 (2002).
[44] L. B. Freund and E. Chason, J. Appl. Phys. **89**, 4866 (2001).
[45] S. C. Seel, C. V. Thompson, S. J. Hearne, and J. A. Floro, J. Appl. Phys. **88**, 7079 (2000).
[46] J. H. van der Merwe, J. Appl. Phys. **41**, 4725 (1970).
[47] J. W. Matthews and A. E. Blakeslee, J. Cryst. Growth **27**, 118 (1974).
[48] F. K. LeGoues, B. S. Meyerson, and J. F. Morar, Phys. Rev. Lett. **66**, 2903 (1991).
[49] J. E. Burke and E. Turnbull, Prog. Met. Phys. **3**, 220 (1952).
[50] J. L. M. Rupp, A. Infortuna, and L. J. Gauckler, Acta Mater. **54**, 1721 (2006).

[51] F. J. Humphreys, *Recrystallization and Grain Growth* (Trans Tech, Stafa-Zurich, Switzerland, 2004), Vol. 2, p. 107.
[52] J. R. Greer, W. C. Oliver, and W. D. Nix, Acta Mater. **53**, 1821 (2005).
[53] S. C. Seel and C. V. Thompson, J. Appl. Phys. **93**, 9038 (2003).
[54] H. Van Swygenhoven, D. Farkas, and A. Caro, Phys. Rev. B **62**, 831 (2000).
[55] J. W. Wyrzykowski and M. W. Grabski, Philos. Mag. A **53**, 505 (1986).
[56] W. W. Mullins, Acta Metall. **6**, 414 (1958).
[57] C. V. Thompson, Annu. Rev. Mater. Sci. **30**, 159 (2000).
[58] J. E. Palmer, C. V. Thompson, and H. I. Smith, J. Appl. Phys. **62**, 2492 (1987).
[59] J. Towers and P. A. Beck, Philos. Mag. **3**, 245 (1954).
[60] W. W. Mullins, J. Appl. Phys. **28**, 333 (1957).
[61] N. E. Munoz, S. R. Gilliss, and C. B. Carter, Surf. Sci. **573**, 391 (2004).
[62] A. D. Rollett and W. W. Mullins, Scr. Mater. **36**, 975 (1997).
[63] S. Mishra, C. Darmann, and K. Lucke, Acta Metall. **32**, 2185 (1984).
[64] H. Makita, S. Hanada, and O. Izumi, Acta Metall. **36**, 403 (1988).
[65] D. P. Norton, A. Goyal, J. D. Budai, D. K. Christen, D. M. Kroeger, E. D. Specht, Q. He, B. Saffian, M. Paranthaman, C. E. Klabunde, D. F. Lee, B. C. Sales, and F. A. List, Science **274**, 755 (1996).
[66] J. M. E. Harper, J. C. Cabral, P. C. Andricacos, L. Gignac, I. C. Noyan, K. P. Rodbell, and C. K. Hu, J. Appl. Phys. **86**, 2516 (1999).
[67] S.-H. Hong and D. N. Lee, Mater. Sci. Eng., A **357**, 75 (2003).
[68] C. G. Dunn and E. F. Koch, Acta Metall. **5**, 548 (1957).
[69] H. J. Frost, C. V. Thompson, and D. T. Walton, Acta Metall. Mater. **40**, 779 (1992).
[70] T. Egami and S. J. L. Billinge, *Underneath the Bragg Peaks: Structural Analysis of Complex Materials* (Elsevier, New York, 2003).